CrossMark

INVITED ARTICLE

Nonmetal element doped g-C_3N_4 with enhanced H_2 evolution under visible light irradiation

Yidan Luo, Jiaming Wang, Shuohan Yu, Yuan Cao, Kaili Ma, Yu Pu, Weixin Zou,[a] and Changjin Tang
Key Laboratory of Mesoscopic Chemistry of MOE, School of Chemistry and Chemical Engineering, Nanjing University, Nanjing 210093, People's Republic of China; and Jiangsu Key Laboratory of Vehicle Emissions Control, Center of Modern Analysis, Nanjing University, Nanjing 210093, People's Republic of China

Fei Gao
Jiangsu Key Laboratory of Vehicle Emissions Control, Center of Modern Analysis, Nanjing University, Nanjing 210093, People's Republic of China; and School of the Environmetal, Nanjing University, Nanjing 210093, People's Republic of China

Lin Dong[b]
Key Laboratory of Mesoscopic Chemistry of MOE, School of Chemistry and Chemical Engineering, Nanjing University, Nanjing 210093, People's Republic of China; and Jiangsu Key Laboratory of Vehicle Emissions Control, Center of Modern Analysis, Nanjing University, Nanjing 210093, People's Republic of China

(Received 1 October 2017; accepted 22 November 2017)

Graphitic carbon nitride (g-C_3N_4) is considered as a promising heterogeneous catalyst for photocatalytic H_2 evolution from water under visible light illustration, and its photocatalytic performance could be controlled through its texture and optical/electronic properties. Herein, we present a facile one-step heating method for the synthesis of B/P/F doped g-C_3N_4 photocatalysts (BCN, PCN, and FCN). The prepared photocatalysts were characterized by XRD, SEM, UV-vis absorption, FTIR, BET, XPS, PL, and photocurrent measurement. The results show that the B/P/F doping increased the interplanar stacking distance of g-C_3N_4, enlarged the optical absorption range, and improved the photocatalytic activity of H_2 evolution. FCN exhibits the highest photocatalytic activity, followed by BCN, and PCN that has the lowest performance. This work studies the doping effects of the nonmetal elements on the photocatalytic activities, the electronic structures as well as the band gaps of g-C_3N_4, to provide a feasible modification pathway to design and synthesize highly efficient photocatalysts.

I. INTRODUCTION

Recently, the aggravated energy and environmental problems have encouraged extensive investigation of new clean energy to replace traditional fossil fuels. Photocatalytic technology is considered as the effective means for converting solar energy to chemical energy. Especially, the photocatalytic hydrogen production from water has become one of the most exciting, sustainable, and environmentally friendly technologies for producing renewable fuels. The photocatalytic hydrogen production could convert solar energy to chemical energy from water, which is potential to replace the traditional fossil fuels.

In 1972, Fujishima and Honda found that Pt and rutile TiO_2 electrodes could photoelectrochemically split water under visible light.[1] Since then, photocatalytic water splitting to produce hydrogen has been considered as an ideal technology. Lots of semiconductor photocatalysts were reported, such as TiO_2,[2] ZnO,[3] Cu_2O,[4] $SrTiO_3$,[5] CdS,[6] MoS_2,[7] and $BiVO_4$,[8] to enhance the optical absorption range of the semiconductors, the separation capability of the photoinduced electron–hole pairs, the photocatalytic stability of the photocatalysts, etc. Recently, it is found that graphitic carbon nitride (g-C_3N_4) with the narrow band gap and high stability is a potential photocatalyst. As a nonmetallic polymeric organic semiconductor, g-C_3N_4 has a layered structure, and it can be easily prepared by thermal polymerization of abundant nitrogen-rich precursors such as urea, thiourea, melamine, dicyandiamide, cyanamide, etc.[9–12] It has been widely investigated for the photocatalytic pollutant degradation, photocatalytic water splitting, CO_2 reduction, etc.[13–15] Nevertheless, the photocatalytic activity of the bulk g-C_3N_4 is very low, due to the high recombination rate as well as few active and adsorption sites exposed.

To increase the photocatalytic activity of g-C_3N_4, many strategies have been taken, such as nanostructure engineering, foreign elements doping, and band

Contributing Editor: Tianyu Liu
Address all correspondence to these authors.
[a]e-mail: zouweixin2011@163.com
[b]e-mail: donglin@nju.edu.cn
DOI: 10.1557/jmr.2017.472

 © Materials Research Society 2018

https://doi.org/10.1557/jmr.2017.472 Published online by Cambridge University Press

alignment by coupling with other semiconductor photocatalysts to improve the electron–hole separation.[16–19] Gu et al.[19] obtained g-C_3N_4 microspheres through a template-free solvothermal approach with postheating treatment. The porous microspheres exhibited narrow band gap and lower resistance, leading to more effective visible-light harvesting and photogenerated charge carrier transport. She et al.[17] reported that α-Fe_2O_3 nanosheets were able to promote exfoliation of g-C_3N_4 in α-Fe_2O_3/g-C_3N_4, and the obtained 2D hybrid exhibited a Z-scheme junction, which effectively suppressed the recombination of electron–hole pairs. Zhang et al.[18] modified g-C_3N_4 with Pt, PtO_x, and CoO_x as redox cocatalysts to directly split pure water photocatalytically.

Doping adds external impurities into semiconductor, which is beneficial to modulate the bulk and surface electronic structures for the manipulation of optical, luminescence, conductive magnetic, or other physical properties.[20] Doping of metal elements, such as Fe, Cu, Co, Ni, etc., could modify the optical and electronic properties of g-C_3N_4 to increase light absorption, reduce band gap, and accelerate charge mobility, which are necessary for pronounced photocatalytic activity.[21,22] Furthermore, due to the advantages of abundance, environmental friendliness, and easy synthesis, the nonmetal element doping is also a successful method to improve the photoactivity of g-C_3N_4. According to the report,[23] the oxygen-functionalized S and P co-doped g-C_3N_4 nanorods had the outstanding visible-light–driven rhodamine B degradation activity. S and P co-doping inhibited the crystal growth of g-C_3N_4 and enhanced the photocatalytic RhB degradation. Zhu et al.[24] proposed that the phosphorus-doped g-C_3N_4 had the increased H_2 evolution rate than pure g-C_3N_4. In addition, other nonmetal elements, such as B, O, and S, were doped and investigated.[25–27] Although there are many reports on nonmetal element doping, the effects of different nonmetal elements on band gap and electronic structure are rarely reported.

In this work, we have successfully fabricated B, P, and F doped g-C_3N_4, by a facile one-step heating method. The doping effects of three different elements on g-C_3N_4 were determined by a series of spectroscopy and electrochemical analysis. The photocatalytic activities were measured by photocatalytic H_2 evolution under visible light illumination. A possible reaction mechanism was proposed.

II. EXPERIMENTAL SECTION

A. Synthesis of photocatalysts

All the chemicals used were of analytical grade, and deionized water was used in all the experiments.

g-C_3N_4 was prepared by calcination using urea as the precursor. Typically, 10 g urea was heated to 520 °C with a heating rate of 5 °C/min and maintained at 520 °C for 2 h in a muffle furnace. The calcination process was carried out in a semiclosed system of a covered crucible to prevent sublimation. The obtained graphitic carbon nitride was labeled as CN.

The nonmetal element doped g-C_3N_4 were synthesized by one-step heating the mixture of urea and the precursor of nonmetal elements (NaH_2PO_4 for element P, $(C_6H_5)_4BNa$ for B, and NH_4F for F). In a typical procedure, 10 g urea and appropriate amounts of the precursor of nonmetal elements were mixed in 20 mL water followed by ultrasonic treatment for 30 min at normal temperature. The mixture was further stirred at room temperature for 30 min and then heated to 80 °C for 3 h to evaporate water to obtain white powders. After grinding, the obtained powders were annealed at 520 °C with a heating rate of 5 °C/min and maintained at 520 °C for 2 h in a muffle furnace. The final products were collected for use without further treatment. The products were named as XCN, X referred to the doped element (B, P, or F) in g-C_3N_4. The proportion of nonmetal elements in urea is 0.05 wt% in the precursors of all the doped samples.

B. Characterization

Scanning electron microscopy (SEM) was performed on a Hitachi S-4800 electron microscope (Hitachi, Tokyo, Japan) operated at a beam energy of 10.0 kV. The catalysts were gold-coated on a Bal-Tec SCD-500 device (Bal-Tec Co., Balzers, Liechtenstein) for 100 s (gold coat 100 Å thick). The crystal structures were identified by X-ray diffraction (XRD) with a Philips X'Pert Pro diffractometer (Philips, Amsterdam, the Netherlands) by Ni-filtered Cu K_α radiation (λ = 0.15418 nm). The powder patterns were measured between 5° and 80°. X-ray photoelectron spectroscopy (XPS) analysis was performed on a PHI 5000 VersaProbe high performance electron spectrometer (ULVAC-PHI, Inc., Chigasaki, Japan) via monochromatic Al K_α radiation (1486.6 eV). The samples were outgassed at room temperature in a UHV chamber ($<5 \times 10^{-7}$ Pa). The charging effect of samples was compensated by all binding energies (BEs) referenced to 284.6 eV of the C 1*s* peak. The baseline of the signals was created considering a Shirley-type background. All the signals were fitted via Gaussian–Lorentzian curves to obtain the BEs of the different element core levels. The Brunauer–Emmett–Teller (BET) surface area was measured by nitrogen adsorption at 77 K on a Micromeritics ASAP-2020 adsorption apparatus (Micromeritics, Norcross, Georgia). The FTIR spectra were collected from 400 to 4000 cm^{-1} at the spectral resolution of 4 cm^{-1} on a Nicolet 5700 FTIR spectrometer (Thermo Electron Corporation, Madison, Wisconsin). The samples (5 mg) were mixed with KBr and pressed into self-supported pellets (50 mg/cm^2). UV-vis diffuse reflectance spectroscopy data were recorded in the range of 200–800 nm by using a Shimadzu UV-2401

https://doi.org/10.1557/jmr.2017.472 Published online by Cambridge University Press

spectrophotometer (Shimadzu Scientific Instruments, Inc., Columbia, Maryland) with the reference of $BaSO_4$. Photoluminescence (PL) spectra were determined on an F-7000 fluorescence spectrophotometer (Hitachi, Tokyo, Japan). The wave length of the excitation light was 325 nm. The experiments were carried out in the solid state. The slit in all measurements was 1.5 nm.

C. Photoelectrochemical measurements

Electrochemical measurements were carried out on a CHI660A electrochemical workstation (Shanghai Chenhua Instrument, Inc., Shanghai, China) using a standard three-electrode cell. The prepared samples were deposited on an In-doped SnO_2-coated glass (ITO glass) electrode as the working electrode with an active area of approximately 1 cm^2, with Pt wire as the counter electrode, saturated calomel electrode (SCE) as the reference electrode, and 0.5 M Na_2SO_4 aqueous solution as the electrolyte. A 300 W Xe lamp with the 420 nm cut-off filter served as a light source. The working electrodes were prepared as follows: 2 mg photocatalyst was grounded with 5 mL ethanol and 10 μL 5% Nafion (DuPont) to make a slurry. Afterward, the slurry was coated onto a 1 × 1.5 cm ITO glass electrode. After air-drying, the working electrode was further dried at 393 K for 2 h to improve adhesion. Finally, a homogeneous film can be obtained. The transient photocurrent densities of the as-prepared electrodes were tested at 0.5 V versus the SCE under visible light irradiation.

D. Photocatalytic H_2 generation testing

The photocatalytic hydrogen evolution reactions were carried out in a top-irradiation type vessel linked to a gas-closed glass system (Ceaulight CEL-SPH2N-D, Ceaulight, Beijing, China) under an irradiation of the 300 W Xe lamp with the 420 nm cut-off filter. 50 mg of the catalyst was dispersed in 100 mL aqueous solution containing triethanolamine (TEOA; 10 vol%) as the sacrificial electron donor. H_2PtCl_6 aqueous solution was added, which was in situ reduced to Pt (3 wt% Pt) during the reaction. The temperature of the solution was kept around 6 °C. The reaction system was sealed and evacuated for 30 min before illumination. The amount of generated hydrogen was automatically collected and determined by using an online gas chromatograph equipped with a thermal conductive detector. Argon was used as the carrier gas for gas chromatography.

III. RESULTS AND DISCUSSION

The crystal structure, texture, and optical and electronic properties of the as-prepared CN, BCN, PCN, and FCN samples were investigated by various characterization methods. The crystalline structures of the as-prepared samples were examined by XRD analysis. The XRD patterns of the three different nonmetal element-doped g-C_3N_4 are shown in Fig. 1(a). Clearly, pure graphitic carbon nitride (CN) shows two XRD peaks at $2\theta = 13.1°$ and 27.5°, which can be perfectly indexed to the (100) and (002) planes of g-C_3N_4, respectively.[28] The (100) plane with the average interlayer distance of $d = 0.675$ nm is related to the in-plane repeating units of the heptazine heteroatom cycles, and the (002) plane with an average distance of $d = 0.326$ nm is attributed to the graphitic layer stacking, similar to graphite.[29–31] Interestingly, when B, P, and F doped, the peak of 27.5° shifts to 27.1°, 27.3°, and 27.0° [Fig. 1(b)], indicating that an increased interplanar stacking distance for BCN, PCN, and FCN, and the dopants are possibly adsorbed in a large hollow space of the interplanar structure.[32] In addition, the peak intensity at about 27.3° follows the order: CN > PCN > BCN > FCN. The decreased peak intensity suggested that the nonmetal element doping suppressed the g-C_3N_4 growth.

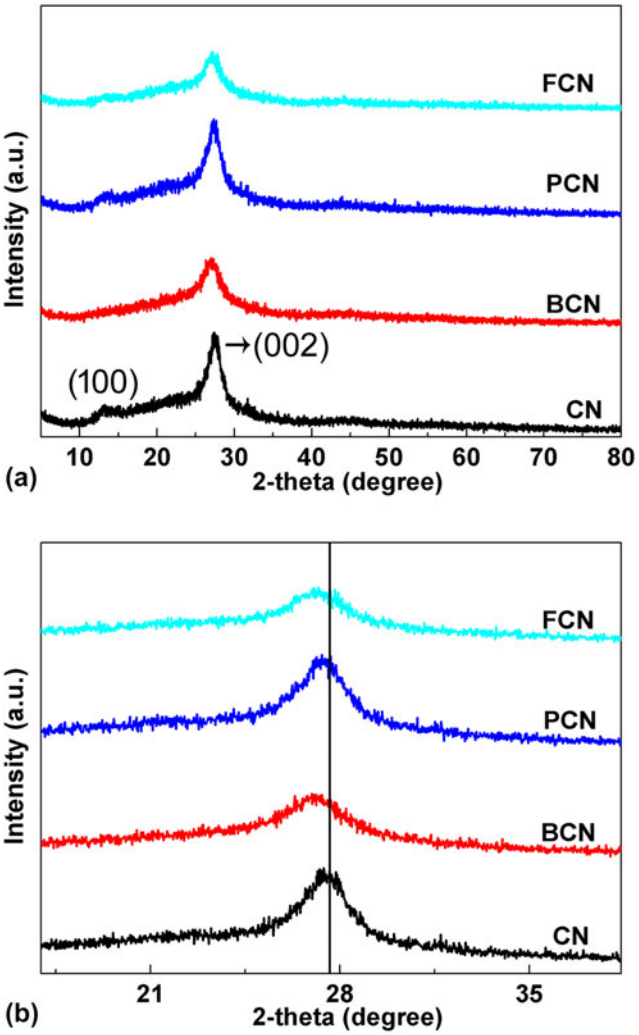


FIG. 1. (a) Powder XRD patterns of CN, BCN, PCN, and FCN samples; (b) the magnified patterns in the range of 17°–38°.

https://doi.org/10.1557/jmr.2017.472 Published online by Cambridge University Press

The molecular structure information of carbon nitride materials was analyzed by using FTIR spectra, as depicted in Fig. 2. The CN, BCN, PCN, and FCN samples exhibit similar FTIR vibration modes. For the pure CN sample, the peak at 809 cm^{-1} is related to the out-of-plane bending vibration of the s-triazine ring.[33] The prominent peaks at 1237, 1319, 1414, 1572, and 1638 cm^{-1} are typical stretching vibration modes of C=N and C–N heterocycles.[34] In addition, the broad peak between 3600 and 2900 cm^{-1} corresponds to the stretching vibration modes of the N–H and O–H stretches of the adsorbed H_2O. Furthermore, all samples have the weak peak at about 2167 cm^{-1}, which belongs to –C≡N or –C≡C– and possibly result from the unreacted intermediate species HO–C≡N or –C≡N on the surface.[35]

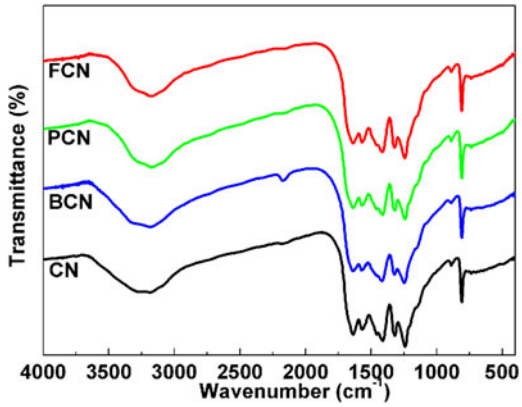


FIG. 2. FTIR spectra of CN, BCN, PCN, and FCN samples.

SEM images were also used to investigate the morphologies of CN, BCN, PCN, and FCN samples. Figure 3 exhibits the SEM images of CN, BCN, PCN, and FCN samples. CN shows a typical ultrathin nanosheet structure. The nanosheets are curling to reduce the surface tension. This phenomenon is found to be identical to the construction of exfoliated carbon scrolls by peeling graphite.[36,37] All the nonmetal element-doped g-C_3N_4 display similar morphologies to pure g-C_3N_4.

To characterize the specific surface area and pore properties of the as-prepared CN, BCN, PCN, and FCN samples, we carried out the N_2 sorption analysis. The nitrogen adsorption–desorption isotherms [Fig. 4(a)], Barrett–Joyner–Halenda (BJH) pore size distribution curves [Fig. 4(b)], and the magnified BJH pore size distribution plots in the region of <10 nm [Fig. 4(c)] of CN, BCN, PCN, and FCN samples reveal that the four samples exhibit type IV isotherms with distinct H3 hysteresis loops, which is a characteristic of mesoporous materials.[38] The type H3 hysteresis loops at $0.70 < P/P_0 < 1.00$ in the isotherms of CN, BCN, PCN, and FCN samples, which are often observed on the aggregates of plate-like particles. The BET specific surface areas of CN, BCN, PCN, and FCN samples are calculated to be 45.1, 40.3, 43.0, and 41.4 m^2/g, respectively. The BET surface areas of nonmetal element doped g-C_3N_4 are slightly lower than those of pure g-C_3N_4. It is inferred that the introduction of nonmetal elements into the urea-condensation reaction may change the texture and the surface morphology, such as collapse of mesopores, and thus the surface area decreased. The pore size distributions of g-C_3N_4 are centered at 3.9 and 32 nm, which represent that there are two kinds of pore structures in g-C_3N_4. The

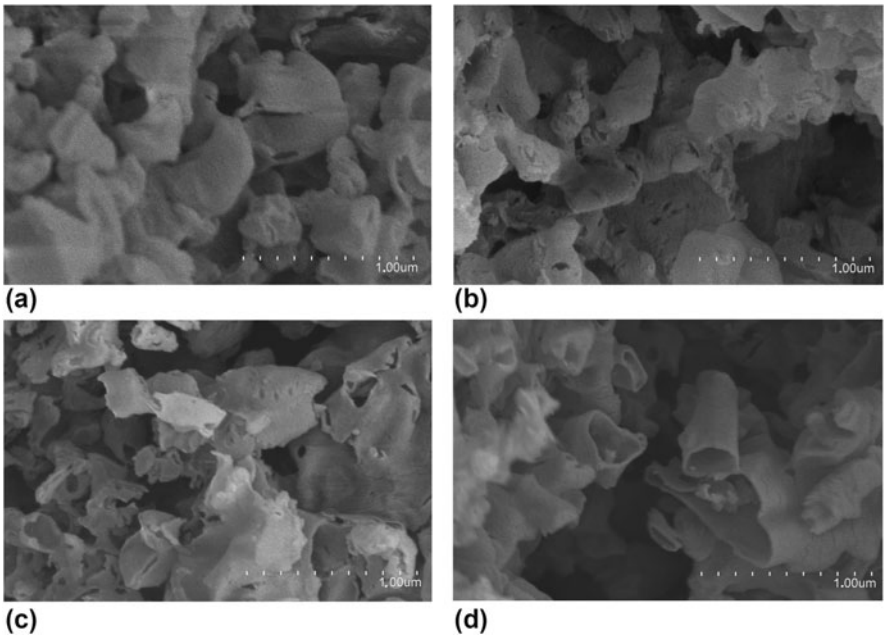


FIG. 3. SEM images of (a) CN, (b) BCN, (c) PCN, and (d) FCN samples.

https://doi.org/10.1557/jmr.2017.472 Published online by Cambridge University Press

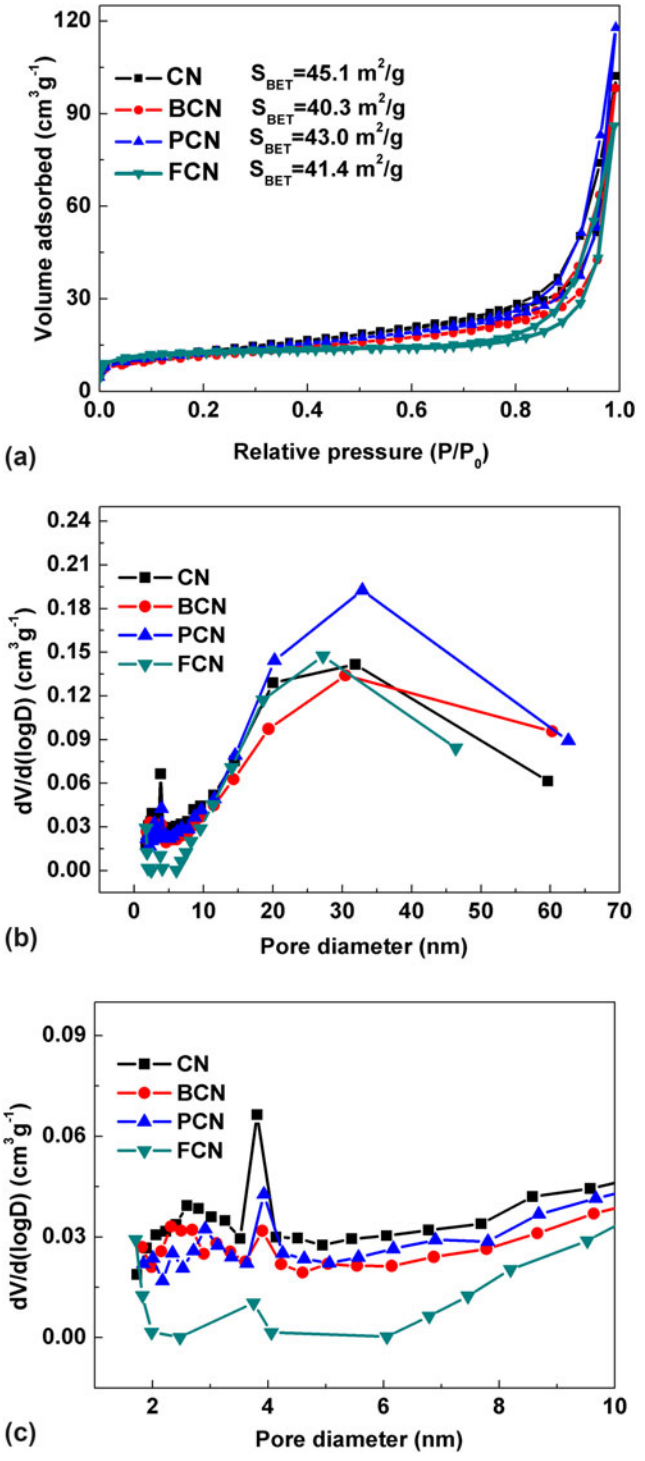


FIG. 4. (a) Nitrogen adsorption–desorption isotherms; (b) BJH pore size distribution plots for CN, BCN, PCN, and FCN samples; (c) The magnified BJH pore size distribution plots in the region of <10 nm.

pore sizes of nonmetal element doped g-C_3N_4 are similar to those of pure g-C_3N_4.

The surface elemental compositions and bonding configurations of CN, BCN, PCN, and FCN were characterized by XPS analysis, and the results are presented. The XPS survey spectra of the as-prepared samples are displayed in Fig. 5(a). The elements C and N are the main constitution in all samples. The oxygen element in CN and BCN is ascribed to the adsorption of oxygen from the atmosphere during the preparation, which is consistent with the reported literature.[39] Because of the low amount of B/P/F, the peaks cannot be detected in the survey spectra, but they can be seen in high-resolution XPS spectra. As shown in Fig. 5(b), the C 1*s* XPS spectrum of g-C_3N_4 could be deconvoluted into two main peaks centered at approximately 284.6 and 288.0 eV.[39] The weak peak at 284.6 eV is attributed to the carbon contamination.[40–42] The strong peak at 288.0 eV corresponds to sp^2-bonded carbon atoms in the heterocycle (N–C=N) of aromatic g-C_3N_4, which is related to the major skeleton carbon in the triazine-base heterocycle.[42,43] As for BCN and PCN, the BEs of the N–C=N groups decrease by 0.2 and 0.1 eV, respectively, while the BE of the N–C=N group in FCN is unchanged compared with that of g-C_3N_4.

The N 1*s* XPS spectra for CN, BCN, PCN, and FCN are displayed in Fig. 5(c). The N 1*s* spectrum of g-C_3N_4 is deconvoluted into four peaks at 398.6, 400.3, 401.2, and 404.2 eV.[44] The dominant peak at 398.6 eV is assigned to sp^2-hybridized nitrogen (pyridine-N) in triazine rings (C–N=C).[45] The C–N=C serves as the main carbon and nitrogen elements in the skeleton, which is considered as the building block of the conjugated system. The peak at 400.3 eV corresponds to ternary nitrogen bonded to carbon atoms (pyrrolic-N) in the form of N–$(C)_3$.[46] The pyridine-N and pyrrolic-N together with N–C=N form the heptazine heterocyclic ring units, which are the main substructure of g-C_3N_4. The peak at 401.2 eV is related to the presence of amino groups (graphitic-N, C–N–H).[47] The small peak at 404.2 eV is originated from the positive charge effect in heterocycles owing to the protonation of g-C_3N_4.[44] Interestingly, after the doping of B, P, and F, the pyridine-N shifts to lower BE from 398.6 to 398.4, 398.5, and 398.5 eV, and the pyrrolic-N shifts from 400.3 eV (CN) to 400.0, 399.9, and 399.7 eV for BCN, PCN, and FCN, respectively. The shift to lower BE is also found in the peaks of graphitic-N. Compared with the BE of 401.2 eV of CN, the BCN, PCN, and FCN shift to lower BEs of 401.0, 400.8, and 400.7 eV, respectively. In conclusion, after the B/P/F doping, the BEs of N 1*s* shift to lower BE, and the pyrrolic-N and graphitic-N shift more compared with pyridine-N. Therefore, the B/P/F doping increases the electron density of pyrrolic-N and graphitic-N.

The B 1*s* XPS spectrum is shown in Fig. 5(d); the peak centered at 191.3 eV is typical BE for B 1*s*.[26] The P 2*p* XPS spectrum of PCN is shown in Fig. 5(e), the peak centered at 132.3 eV is assigned to P $2p_{3/2}$, while the peak centered at 133.2 eV is related to P $2p_{1/2}$.[29] Fig. 5(f) presents the F 1*s* XPS spectrum of FCN. The peak at

https://doi.org/10.1557/jmr.2017.472 Published online by Cambridge University Press

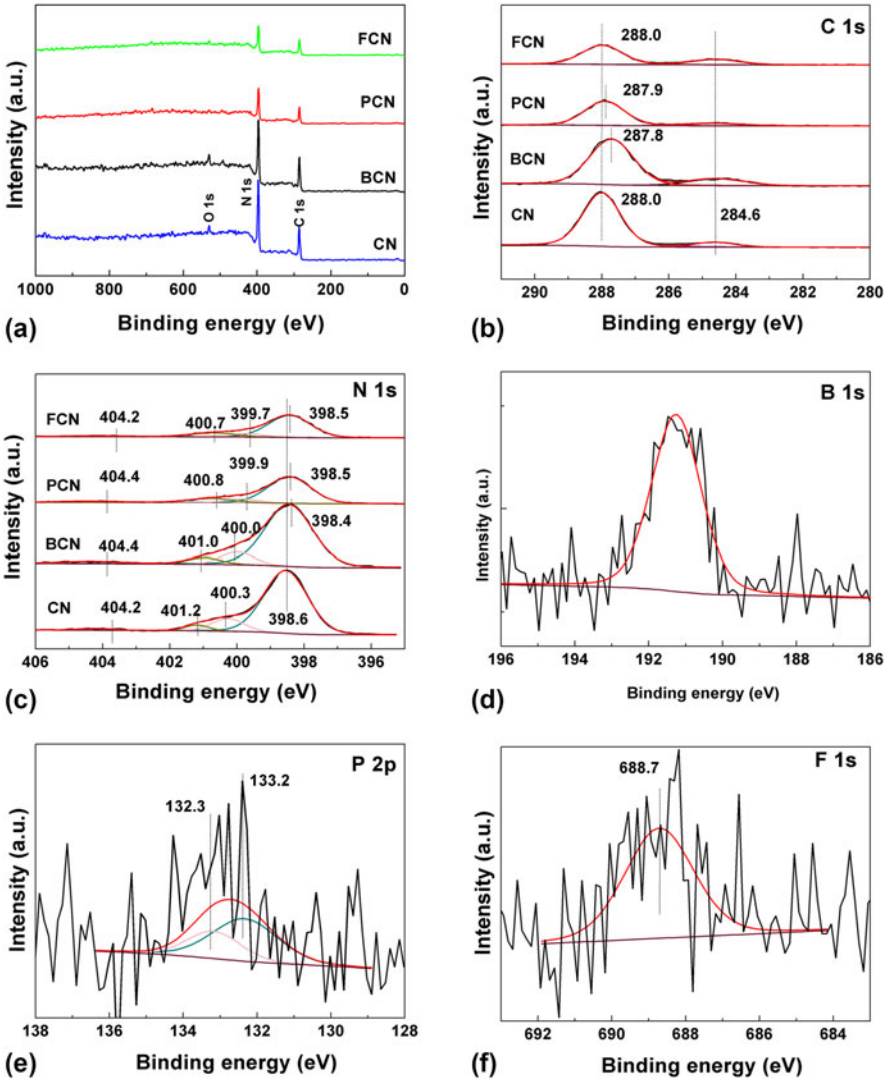


FIG. 5. (a) XPS survey spectra of the as-prepared samples; high-resolution XPS spectra of CN, BCN, PCN, and FCN: (b) C 1*s*, (c) N 1*s*, (d) B 1*s*, (e) P 2*p*, and (f) F 1*s*.

688.7 eV is assigned to the typical BE of F 1*s*.[48] On the basis of XPS analysis for the corresponding samples, the contents of B in BCN, P in PCN and F in FCN are 1.35, 0.72, and 1.08 atom%, respectively.

The introduction of nonmetal elements into the graphitic carbon nitride polymeric skeleton changes the structure and electronic aspects and thus the resultant optical properties. To gather more insights on nonmetal element doping effects on the physicochemical properties of graphitic carbon nitride, the optical properties of the samples were investigated in detail. The absorption spectra of CN, BCN, PCN, and FCN samples are demonstrated in Fig. 6(a). All samples show the typical absorption with a sharp light absorption band threshold, which results from the charge transfer from the valence band (VB) to the conduction band (CB) of the semiconductor. Pure g-C_3N_4 shows a sharp absorption band threshold at about 479 nm. After the doping process, BCN, PCN, and FCN samples show enhanced absorption in visible light region with a perceptible red-shift of the optical absorption edges. This phenomenon is very common for doping modifications of the semiconductors.[49,50] The semiconductor photoexcitation strongly depends on the wave length of excitation light and the band gap of the semiconductor. The calculated band gap energies of CN, BCN, PCN, and FCN samples are in the inset picture of Fig. 6(a). The calculation of band gap energies is based on Eq. (1):

$$\alpha h\nu = A\left(h\nu - E_g\right)^{(n/2)} \quad , \qquad (1)$$

where α represents the absorption coefficient, h is the Planck's constant, ν is the light frequency, and A is the energy-independent constant.[51] It should be noted that

https://doi.org/10.1557/jmr.2017.472 Published online by Cambridge University Press

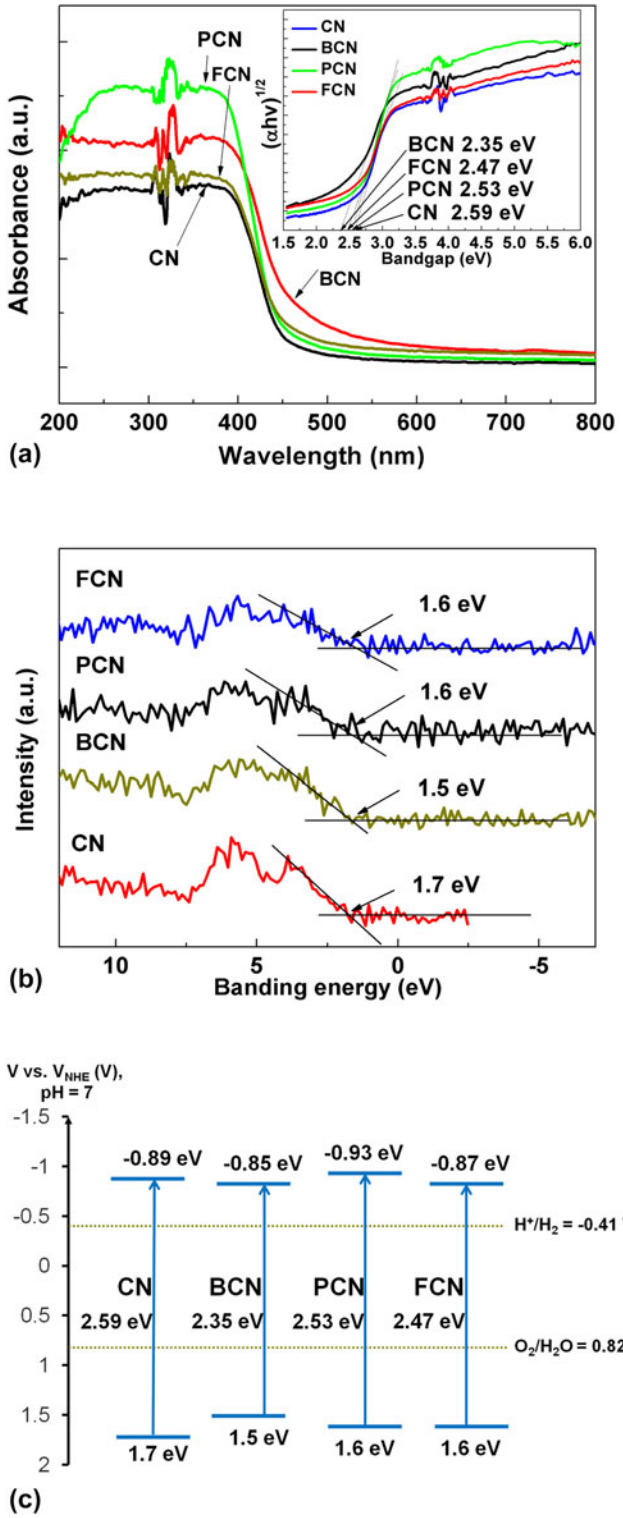


FIG. 6. (a) UV-vis absorption spectra of the as-prepared samples. The inset shows the band gap energies of CN, BCN, PCN, and FCN; (b) VB XPS of CN, BCN, PCN, and FCN; (c) Band gap structures of CN, BCN, PCN, and FCN.

the value of n is determined by the type of optical transition of the semiconductor ($n = 1$ for direct transition and $n = 4$ for indirect transition).[52] Because n value of graphitic carbon nitride is 4, the E_g of samples can be determined by the tangent lines of $(\alpha h\nu)^{(1/2)}$ versus $(h\nu)$.[53] The band gap energy of CN is 2.59 eV, while the band gap energies of BCN, PCN, and FCN samples are 2.35, 2.53, and 2.47 eV, respectively. It's confirmed that the B/P/F doping process can decrease the band gap energy and increase the light absorption region, which could result in higher photocatalytic activity.

The VB XPS of CN, BCN, PCN, and FCN samples are shown in Fig. 6(b). As observed in Fig. 6(b), the obtained VB maxima of CN is 1.7 eV, while the VB maxima of BCN, PCN, and FCN are 1.5, 1.6, 1.6 eV, respectively. Compared with g-C_3N_4 (1.7 eV), the VB position of BCN (1.5 eV) shifts up 0.2 eV and that of PCN and FCN shift up 0.1 eV. Based on the VB potentials and band gaps, the CB of CN, BCN, PCN, and FCN are estimated to be −0.89, 0.85, −0.93, and −0.87 eV, respectively. As we known, the potentials of VB and CB can determine the oxidizing and reducing ability of semiconductors. The band gap structures are shown in Fig. 6(c), and the negative shift of CB of PCN can make the electron more reductive.

The photocatalytic activities of the as-prepared CN, BCN, PCN, and FCN samples were examined by photocatalytic H_2 evolution under visible light irradiation ($\lambda > 420$ nm), using 10 vol% triethanolamine as a sacrificial reagent and 3 wt% Pt as a cocatalyst. In Fig. 7(a), there are clear differences in the H_2 evolution amount for the as-prepared CN, BCN, PCN, and FCN samples. The H_2 evolution amount of CN is determined as 2158 μmol/g in 5 h, while FCN has 3726 μmol/g and 1.72 times higher than pure g-C_3N_4. The BCN possesses the 3522 μmol/g H_2 evolution amount. The H_2 evolution amount of PCN (2500 μmol/g) is still higher than that of the pure g-C_3N_4 (2158 μmol/g). It is noteworthy that the H_2 evolution amounts of all the nonmetal doped g-C_3N_4 are higher than those of the pure g-C_3N_4, directly certifying the positive improvements of the B/P/F doping in the photocatalytic activities. The order for the amount of photocatalytic H_2 evolution is FCN > BCN > PCN > CN. Figure 7(b) shows the photocatalytic H_2 evolution rates for the CN, BCN, PCN, and FCN samples under visible light irradiation. The rates for CN, BCN, PCN, and FCN samples are 431.6, 704.5, 500.0, and 745.2 μmol/(g h), respectively.

The PL spectroscopy is a well-known technique to study both the interface charge carrier transfer and the electron–hole pair recombination. It was reported that the PL resulted from the following process. Light is absorbed by the photocatalyst and the excess energy is given to electrons, leading to the electrons within the photocatalyst to transfer into permissible excited states. Afterward, electrons return to the equilibrium states, and light is emitted.[54,55] Figure 7(c) shows that all photocatalysts have similar emission trends centered at about 460 nm.

https://doi.org/10.1557/jmr.2017.472 Published online by Cambridge University Press

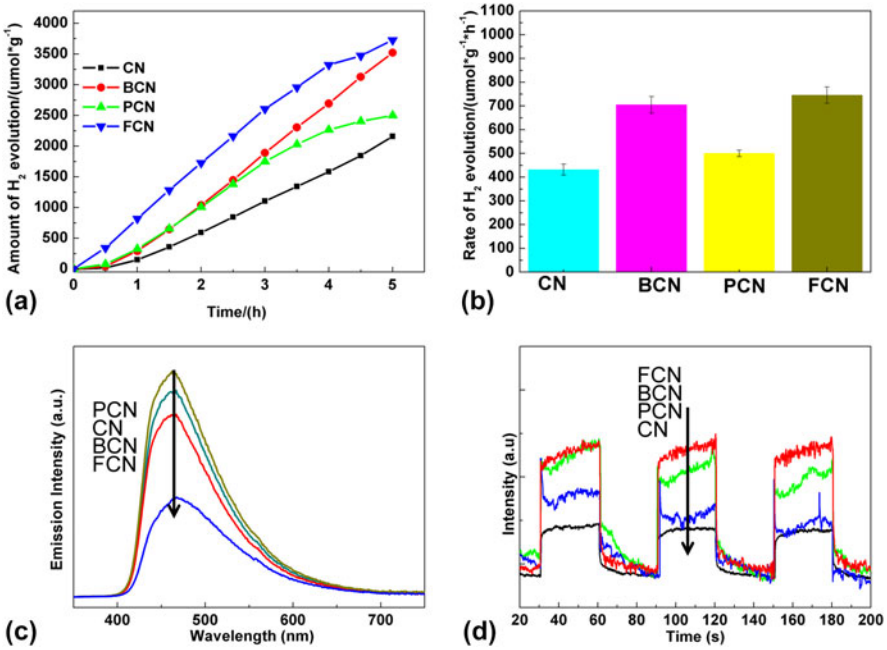


FIG. 7. (a) The amount of H_2 evolution of the as-prepared samples under visible light irradiation ($\lambda > 420$ nm); (b) Rate of photocatalytic H_2 production over the CN, BCN, PCN, and FCN under visible light irradiation ($\lambda > 420$ nm); (c) PL spectra of CN, BCN, PCN, and FCN samples; (d) Transient photocurrent density versus the time of CN, BCN, PCN, and FCN samples.

When F was doped in g-C_3N_4, the intensity of this emission peak drops significantly. This is ascribed to the promoted electron relocalization on the surface terminal after doping.[24,56] This indicates that the B and F doping lead to an improved separation efficiency of the photoinduced electron–hole pairs under visible-light illumination. The PL peak intensity was in the order of PCN > CN > BCN > FCN, indicating that the order of the electron–hole recombination rate were PCN > CN > BCN > FCN. However, the electron–hole recombination order was not consistent with the photocatalytic activity. It was reported that PL spectra are also sensitive to energy levels of the exciton structures, impurities, and crystalline quality.[57,58] According to the above literature, it was considered that the inconsistency of PL intensity and phtocatalytic activity might result from the relative vacancy concentration.

The photocurrent responses of CN, BCN, PCN, and FCN samples under visible light were performed to further identify the interfacial charge transfer and recombination rates occurring in the three-electrode systems. As observed in Fig. 7(d), the doped g-C_3N_4 photocatalysts exhibit higher photocurrent density than the pure g-C_3N_4, indicating that the nonmetal element doping can more efficiently increase the interfacial charge transfer. The FCN produces a higher photocurrent than BCN, PCN, and CN samples under the same condition, suggesting that it has lower recombination rate and the superior photocatalytic activity enhancement. The intensity of photocurrent density is in the following order: CN < PCN < BCN < FCN, which is consistent with the photocatalytic H_2 evolution activity.

Generally, the photocatalysis process is believed to be of three steps: the photoexcitation of semiconductor, the separation and transfer of photoinduced charge carriers, and the reaction between the charge carriers and reactant molecules. The bandgap structure of the semiconductor is the main factor for photoexcitation. The nonmetal elements (B, P, and F) have an influence on the intrinsic electronic and band structure modulation of g-C_3N_4. The CB and VB potentials of the BCN are −0.85 and 1.5 eV, respectively, while those of PCN are −0.93 and 1.6 eV and FCN are −0.87 and 1.6 eV [Fig. 6(c)]. The B/P/F doped g-C_3N_4 with a narrow band gap would harvest more visible-light photons and produce more photogenerated carriers than pure g-C_3N_4. The negative shift of the CB of PCN can make the electron more reductive.

After photoexcitation, the photocatalytic activity depends on the competition between photogenerated carrier recombination and trapping. The low recombination rate can facilitate the separation of electron–hole pairs. From the transient photocurrent response under visible light of the as-prepared samples, it is observed that the FCN shows the fastest photogenerated electron transfer.

Additionally, it can be known that the large BET specific surface area is important to photocatalytic activity. From Fig. 4(a), it can be found that the specific surface areas of BCN, PCN, and FCN are 40.3, 43.0, and 41.4 m^2/g, respectively, which are very close to CN (45.1 m^2/g). Thus, specific surface areas are not the

https://doi.org/10.1557/jmr.2017.472 Published online by Cambridge University Press

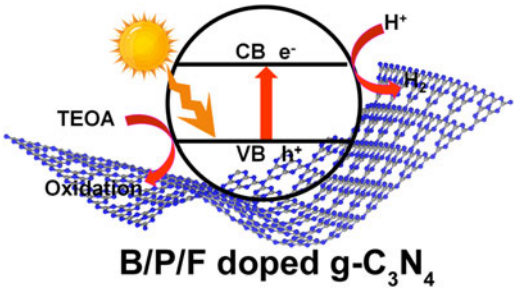


FIG. 8. Proposed reaction mechanism for photocatalytic H_2 evolution on BCN, PCN, and FCN.

critical factor to determine the catalytic performances of the photocatalysts.

According to the above results, the mechanisms for the photocatalytic H_2 production by BCN, PCN, and FCN are proposed in Fig. 8. When BCN, PCN, and FCN are irradiated by light with energy larger than the band gap, the excited charges are generated, separated, and migrated to the surface. Then the photogenerated charge carriers transfer to the catalyst surface. The electrons reduce H_2O to generate H_2. At the same time, the holes oxidize the TEOA to restrain the charge recombination and thus promote the photocatalytic activities.

IV. CONCLUSIONS

In this contribution, we have successfully fabricated B, P, and F doped g-C_3N_4 by a facile one-step heating method and investigated the different effects of the dopants on the electronic structures and band gaps. The photocatalytic H_2 evolution was in the order of FCN > BCN > PCN > CN. The B/P/F doping decreases the band gap of g-C_3N_4, enlarges the optical absorption range, and thus produces more photogenerated carriers, which lead to the increase of photocatalytic H_2 evolution activity. Compared with the P dopant, the B and F doped g-C_3N_4 shows the more decreased band gap, faster photogenerated carrier separation, and thus better photocatalytic performance.

ACKNOWLEDGMENTS

This work was financially supported by National 863 plans projects (2015AA03A401), the Natural Science Foundation of Jiangsu Province (BK20161392), and National Natural Science Foundation of China (21670182, 21573105, and 21707066).

REFERENCES

1. A. Fujishima and K. Honda: Electrochemical photolysis of water at a semiconductor electrode. *Nature* **238**, 37–38 (1972).
2. Y.D. Luo, S.H. Yu, B. Li, L.H. Dong, F. Wang, M.G. Fan, and F.Y. Zhang: Synthesis of (Ag,F)-modified anatase TiO_2 nanosheets and their enhanced photocatalytic activity. *New J. Chem.* **40**, 2135–2144 (2016).
3. J.C. Sin, S.M. Lam, I. Satoshi, K.T. Lee, and A.R. Mohamed: Sunlight photocatalytic activity enhancement and mechanism of novel europium-doped ZnO hierarchical micro/nanospheres for degradation of phenol. *Appl. Catal., B* **148–149**, 258–268 (2014).
4. Y. Luo, Q. Huang, B. Li, L. Dong, M. Fan, and F. Zhang: Synthesis and characterization of Cu_2O–modified Bi_2O_3 nanospheres with enhanced visible light photocatalytic activity. *Appl. Surf. Sci.* **357**, 1072–1079 (2015).
5. L. Dong, H. Shi, K. Cheng, Q. Wang, W. Weng, and W. Han: Shape-controlled growth of $SrTiO_3$ polyhedral submicro/nanocrystals. *Nano Res.* **7**, 1311–1318 (2014).
6. K. Ma, O. Yehezkeli, D.W. Domaille, H.H. Funke, and J.N. Cha: Enhanced hydrogen production from DNA-assembled Z-scheme TiO_2-CdS photocatalyst systems. *Angew. Chem., Int. Ed.* **54**, 11490–11494 (2015).
7. K.L. Ai, C.P. Ruan, M.X. Shen, and L.H. Lu: MoS_2 nanosheets with widened interlayer spacing for high-efficiency removal of mercury in aquatic systems. *Adv. Funct. Mater.* **26**, 5542–5549 (2016).
8. R. Negishi, S.i. Naya, and H. Tada: Visible light-driven selective aerobic oxidation of benzylalcohols to benzaldehydes by a $Cu(acac)_2$-$BiVO_4$-admicelle three-component heterosupramolecular photocatalyst. *J. Phys. Chem. C* **119**, 11771–11776 (2015).
9. Q. Su, J. Sun, J. Wang, Z. Yang, W. Cheng, and S. Zhang: Urea-derived graphitic carbon nitride as an efficient heterogeneous catalyst for CO_2 conversion into cyclic carbonates. *Catal. Sci. Technol.* **4**, 1556 (2014).
10. Z. Zhou, J. Wang, J. Yu, Y. Shen, Y. Li, A. Liu, S. Liu, and Y. Zhang: Dissolution and liquid crystals phase of 2D polymeric carbon nitride. *J. Am. Chem. Soc.* **137**, 2179–2182 (2015).
11. Y. Zhang, J. Liu, G. Wu, and W. Chen: Porous graphitic carbon nitride synthesized via direct polymerization of urea for efficient sunlight-driven photocatalytic hydrogen production. *Nanoscale* **4**, 5300–5303 (2012).
12. H.J. Li, B.W. Sun, L. Sui, D.J. Qian, and M. Chen: Preparation of water-dispersible porous g-C_3N_4 with improved photocatalytic activity by chemical oxidation. *Phys. Chem. Chem. Phys.* **17**, 3309–3315 (2015).
13. M. Zhang, W. Jiang, D. Liu, J. Wang, Y. Liu, Y. Zhu, and Y. Zhu: Photodegradation of phenol via C_3N_4-agar hybrid hydrogel 3D photocatalysts with free separation. *Appl. Catal., B* **183**, 263–268 (2016).
14. J. Qin, J. Huo, P. Zhang, J. Zeng, T. Wang, and H. Zeng: Improving the photocatalytic hydrogen production of Ag/g-C_3N_4 nanocomposites by dye-sensitization under visible light irradiation. *Nanoscale* **8**, 2249–2259 (2016).
15. R. Kuriki, O. Ishitani, and K. Maeda: Unique solvent effects on visible-light CO_2 reduction over ruthenium(II)-complex/carbon nitride hybrid photocatalysts. *ACS Appl. Mater. Interfaces* **8**, 6011–6018 (2016).
16. T.Y. Ma, J.R. Ran, S. Dai, M. Jaroniec, and S.Z. Qiao: Phosphorus-doped graphitic carbon nitrides grown in situ on carbon-fiber paper: Flexible and reversible oxygen electrodes. *Angew. Chem., Int. Ed.* **54**, 4646–4650 (2015).
17. X. She, J. Wu, H. Xu, J. Zhong, Y. Wang, Y. Song, K. Nie, Y. Liu, Y. Yang, M.T.F. Rodrigues, R. Vajtai, J. Lou, D. Du, H. Li, and P.M. Ajayan: High efficiency photocatalytic water splitting using 2D α-Fe_2O_3/g-C_3N_4 Z-scheme catalysts. *Adv. Energy Mater.* **7**, 1700025 (2017).
18. G. Zhang, Z.A. Lan, L. Lin, S. Lin, and X. Wang: Overall water splitting by Pt/g-C_3N_4 photocatalysts without using sacrificial agents. *Chem. Sci.* **7**, 3062–3066 (2016).
19. Q. Gu, Y. Liao, L. Yin, J. Long, X. Wang, and C. Xue: Template-free synthesis of porous graphitic carbon nitride microspheres for

https://doi.org/10.1557/jmr.2017.472 Published online by Cambridge University Press

enhanced photocatalytic hydrogen generation with high stability. *Appl. Catal., B* **165**, 503–510 (2015).
20. S.C. Yan, Z.S. Li, and Z.G. Zou: Photodegradation of rhodamine B and methyl orange over boron-doped g-C_3N_4 under visible light irradiation. *Langmuir* **26**, 3894–3901 (2010).
21. Z. Ding, X. Chen, M. Antonietti, and X. Wang: Synthesis of transition metal-modified carbon nitride polymers for selective hydrocarbon oxidation. *ChemSusChem* **4**, 274–281 (2011).
22. B. Yue, Q. Li, H. Iwai, T. Kako, and J. Ye: Hydrogen production using zinc-doped carbon nitride catalyst irradiated with visible light. *Sci. Technol. Adv. Mater.* **12**, 034401 (2011).
23. S.Z. Hu, L. Ma, Y. Xie, F.Y. Li, Z.P. Fan, F. Wang, Q. Wang, Y.J. Wang, X.X. Kang, and G. Wu: Hydrothermal synthesis of oxygen functionalized S–P codoped g-C_3N_4 nanorods with outstanding visible light activity under anoxic conditions. *Dalton Trans.* **44**, 20889–20897 (2015).
24. Y.P. Zhu, T.Z. Ren, and Z.Y. Yuana: Mesoporous phosphorus-doped g-C_3N_4 nanostructured flowers with superior photocatalytic hydrogen evolution performance. *ACS Appl. Mater. Interfaces* **7**, 16850–16856 (2015).
25. Y.Y. Bu and Z.Y. Chen: Effect of oxygen-doped C_3N_4 on the separation capability of the photoinduced electron-hole pairs generated by O-C_3N_4@TiO_2 with quasi–shell–core nanostructure. *Electrochim. Acta* **144**, 42–49 (2014).
26. C.H. Lu, R.Y. Chen, X. Wu, M.F. Fan, Y.H. Liu, Z.G. Le, S.J. Jiang, and S.Q. Song: Boron doped g-C_3N_4 with enhanced photocatalytic UO_2^{2+} reduction performance. *Appl. Surf. Sci.* **360**, 1016–1022 (2016).
27. H.J. Kong, D.H. Won, J. Kim, and S.I. Woo: Sulfur-doped g-C_3N_4/$BiVO_4$ composite photocatalyst for water oxidation under visible light. *Chem. Mater.* **28**, 1318–1324 (2016).
28. Z.A. Lan, G. Zhang, and X. Wang: A facile synthesis of Br-modified g-C_3N_4 semiconductors for photoredox water splitting. *Appl. Catal., B* **192**, 116–125 (2016).
29. H.Q. Ma, Y. Li, S. Li, and N. Liu: Novel P–O codoped g-C_3N_4 with large specific surface area: Hydrothermal synthesis assisted by dissolution-precipitation process and their visible light activity under anoxic conditions. *Appl. Surf. Sci.* **357**, 131–138 (2015).
30. X. Wang, K. Maeda, A. Thomas, K. Takanabe, G. Xin, J.M. Carlsson, K. Domen, and M. Antonietti: A metal-free polymeric photocatalyst for hydrogen production from water under visible light. *Nat. Mater.* **8**, 76–80 (2009).
31. J. Gracia and P. Kroll: Corrugated layered heptazine-based carbon nitride: The lowest energy modifications of C_3N_4 ground state. *J. Mater. Chem.* **19**, 3013–3019 (2009).
32. X.G. Ma, Y.H. Lv, J. Xu, Y.F. Liu, R.Q. Zhang, and Y.F. Zhu: A strategy of enhancing the photoactivity of g-C_3N_4 via doping of nonmetal elements: A first-principles study. *J. Phys. Chem. C* **116**, 23485–23493 (2012).
33. H. Li, S. Gan, H. Wang, D. Han, and L. Niu: Intercorrelated superhybrid of AgBr supported on graphitic-C_3N_4-decorated nitrogen-doped graphene: High engineering photocatalytic activities for water purification and CO_2 reduction. *Adv. Mater.* **27**, 6906–6913 (2015).
34. K.C. Christoforidis, T. Montini, E. Bontempi, S. Zafeiratos, J.J. Delgado Jaen, and P. Fornasiero: Synthesis and photocatalytic application of visible-light active beta-Fe_2O_3/g-C_3N_4 hybrid nanocomposites. *Appl. Catal., B* **187**, 171–180 (2016).
35. G. Zhang, J. Zhang, M. Zhang, and X. Wang: Polycondensation of thiourea into carbon nitride semiconductors as visible light photocatalysts. *J. Mater. Chem.* **22**, 8083–8091 (2012).
36. Z.Z. Lin and X.C. Wang: Nanostructure engineering and doping of conjugated carbon nitride semiconductors for hydrogen photosynthesis. *Angew. Chem., Int. Ed.* **52**, 1735–1738 (2013).
37. T.G. Xu, L.W. Zhang, H.Y. Cheng, and Y.F. Zhu: Significantly enhanced photocatalytic performance of ZnO via graphene hybridization and the mechanism study. *Appl. Catal., B* **101**, 382–387 (2011).
38. S.W. Hu, L.W. Yang, Y. Tian, X.L. Wei, J.W. Ding, J.X. Zhong, and P.K. Chu: Simultaneous nanostructure and heterojunction engineering of graphitic carbon nitride via in situ Ag doping for enhanced photoelectrochemical activity. *Appl. Catal., B* **163**, 611–622 (2015).
39. W.J. Ong, L.K. Putri, L.L. Tan, S.P. Chai, and S.T. Yong: Heterostructured AgX/g-C_3N_4 (X = Cl and Br) nanocomposites via a sonication-assisted deposition-precipitation approach: Emerging role of halide ions in the synergistic photocatalytic reduction of carbon dioxide. *Appl. Catal., B* **180**, 530–543 (2016).
40. M. Lu, Z. Pei, S. Weng, W. Feng, Z. Fang, Z. Zheng, M. Huang, and P. Liu: Constructing atomic layer g-C_3N_4-CdS nanoheterojunctions with efficiently enhanced visible light photocatalytic activity. *Phys. Chem. Chem. Phys.* **16**, 21280–21288 (2014).
41. Y. Cui, Z. Ding, X. Fu, and X. Wang: Construction of conjugated carbon nitride nanoarchitectures in solution at low temperatures for photoredox catalysis. *Angew. Chem., Int. Ed.* **51**, 11814–11818 (2012).
42. Z.a. Huang, Q. Sun, K. Lv, Z. Zhang, M. Li, and B. Li: Effect of contact interface between TiO_2 and g-C_3N_4 on the photoreactivity of g-C_3N_4/TiO_2 photocatalyst: (0 0 1) versus (1 0 1) facets of TiO_2. *Appl. Catal., B* **164**, 420–427 (2015).
43. L. Zhao, L. Zhang, H. Lin, Q. Nong, M. Cui, Y. Wu, and Y. He: Fabrication and characterization of hollow $CdMoO_4$ coupled g-C_3N_4 heterojunction with enhanced photocatalytic activity. *J. Hazard. Mater.* **299**, 333–342 (2015).
44. C. Li, Y. Du, D. Wang, S. Yin, W. Tu, Z. Chen, M. Kraft, G. Chen, and R. Xu: Unique P–Co–N surface bonding states constructed on g-C_3N_4 nanosheets for drastically enhanced photocatalytic activity of H_2 evolution. *Adv. Funct. Mater.* **27**, 1304328 (2017).
45. J. Yan, H. Wu, H. Chen, Y. Zhang, F. Zhang, and S.F. Liu: Fabrication of TiO_2/C_3N_4 heterostructure for enhanced photocatalytic Z-scheme overall water splitting. *Appl. Catal., B* **191**, 130–137 (2016).
46. N. Tian, Y. Zhang, C. Liu, S. Yu, M. Li, and H. Huang: g-C_3N_4/$Bi_4O_5I_2$ 2D–2D heterojunctional nanosheets with enhanced visible-light photocatalytic activity. *RSC Adv.* **6**, 10895–10903 (2016).
47. K. Dai, L. Lu, C. Liang, G. Zhu, Q. Liu, L. Geng, and J. He: A high efficient graphitic-C_3N_4/BiOI/graphene oxide ternary nanocomposite heterostructured photocatalyst with graphene oxide as electron transport buffer material. *Dalton Trans.* **44**, 7903–7910 (2015).
48. Y. Wang, Y. Di, M. Antonietti, H. Li, X. Chen, and X. Wang: Excellent visible-light photocatalysis of fluorinated polymeric carbon nitride solids. *Chem. Mater.* **22**, 5119–5121 (2010).
49. J.H. Li, B.A. Shen, Z.H. Hong, B.Z. Lin, B.F. Gao, and Y.L. Chen: A facile approach to synthesize novel oxygen-doped g-C_3N_4 with superior visible-light photoreactivity. *Chem. Commun.* **48**, 12017–12019 (2012).
50. D.H. Lan, H.T. Wang, L. Chen, C.T. Au, and S.F. Yin: Phosphorous-modified bulk graphitic carbon nitride: Facile preparation and application as an acid-base bifunctional and efficient catalyst for CO_2 cycloaddition with epoxides. *Carbon* **100**, 81–89 (2016).
51. Q. Cao, R. Che, and N. Chen: Scalable synthesis of Cu_2S double-superlattice nanoparticle systems with enhanced UV/visible-light-driven photocatalytic activity. *Appl. Catal., B* **162**, 187–195 (2015).

https://doi.org/10.1557/jmr.2017.472 Published online by Cambridge University Press

52. J. Liang, G. Zhu, P. Liu, X. Luo, C. Tan, L. Jin, and J. Zhou: Synthesis and characterization of Fe-doped β-Bi_2O_3 porous microspheres with enhanced visible light photocatalytic activity. *Superlattices Microstruct.* **72**, 272–282 (2014).
53. J. Ma, X. Tan, F. Jiang, and T. Yu: Graphitic C_3N_4 nanosheet-sensitized brookite TiO_2 to achieve photocatalytic hydrogen evolution under visible light. *Catal. Sci. Technol.* **7**, 3275–3282 (2017).
54. X. Xing, R. Liu, X. Yu, G. Zhang, H. Cao, J. Yao, B. Ren, Z. Jiang, and H. Zhao: Self-assembly of CdS quantum dots with polyoxometalate encapsulated gold nanoparticles: Enhanced photocatalytic activities. *J. Mater. Chem. A* **1**, 1488–1494 (2013).
55. W.X. Zou, L. Zhang, L.C. Liu, X.B. Wang, J.F. Sun, S.G. Wu, Y. Deng, C.J. Tang, F. Gao, and L. Dong: Engineering the Cu_2O-reduced graphene oxide interface to enhance photocatalytic degradation of organic pollutants under visible light. *Appl. Catal., B* **181**, 495–503 (2016).
56. X. Wang, K. Maeda, X. Chen, K. Takanabe, K. Domen, Y. Hou, X. Fu, and M. Antonietti: Polymer semiconductors for artificial photosynthesis: Hydrogen evolution by mesoporous graphitic carbon nitride with visible light. *J. Am. Chem. Soc.* **131**, 1680–1681 (2009).
57. A. White, E. Williams, P. Porteous, and C. Hilsum: Applications of photoluminescence excitation spectroscopy to the study of indium gallium phosphide alloys. *J. Phys. D: Appl. Phys.* **3**, 1322–1328 (1970).
58. W. Yu, K. Jiang, J. Wu, J. Gan, M. Zhu, Z. Hu, and J. Chu: Electronic structures and excitonic transitions in nanocrystalline iron-doped tin dioxide diluted magnetic semiconductor films: An optical spectroscopic study. *Phys. Chem. Chem. Phys.* **13**, 6211–6222 (2011).

https://doi.org/10.1557/jmr.2017.472 Published online by Cambridge University Press